

Accepted Manuscript

Crystal structure and magnetic-dipole emissions of $\text{Sr}_2\text{CaWO}_6: \text{RE}^{3+}$ (RE=Dy, Sm and Eu) phosphors

Xiaoyu Song, Xianxian Wang, Xuewen Xu, Xin Liu, Xiaoli Ge, Fanbin Meng



PII: S0925-8388(17)34498-5

DOI: [10.1016/j.jallcom.2017.12.302](https://doi.org/10.1016/j.jallcom.2017.12.302)

Reference: JALCOM 44388

To appear in: *Journal of Alloys and Compounds*

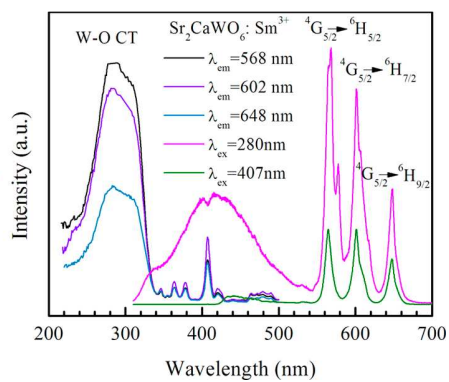
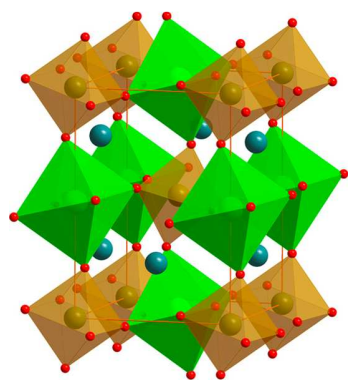
Received Date: 21 October 2017

Revised Date: 18 December 2017

Accepted Date: 25 December 2017

Please cite this article as: X. Song, X. Wang, X. Xu, X. Liu, X. Ge, F. Meng, Crystal structure and magnetic-dipole emissions of $\text{Sr}_2\text{CaWO}_6: \text{RE}^{3+}$ (RE=Dy, Sm and Eu) phosphors, *Journal of Alloys and Compounds* (2018), doi: 10.1016/j.jallcom.2017.12.302.

This is a PDF file of an unedited manuscript that has been accepted for publication. As a service to our customers we are providing this early version of the manuscript. The manuscript will undergo copyediting, typesetting, and review of the resulting proof before it is published in its final form. Please note that during the production process errors may be discovered which could affect the content, and all legal disclaimers that apply to the journal pertain.



Crystal structure and magnetic-dipole emissions of Sr_2CaWO_6 : RE^{3+} (RE=Dy, Sm and Eu) phosphors

Xiaoyu Song, Xianxian Wang, Xuewen Xu*, Xin Liu, Xiaoli Ge, Fanbin Meng

School of Materials Science and Engineering, Hebei University of Technology, Tianjin
300130, P. R. China

Corresponding author: X.W. Xu, Tel: +86-22-60204805, Fax: +86-22-60202660, E-mail:

xuxuewen@hebut.edu.cn.

E-mail:

sxyhebut@163.com

15022729860@163.com

xuxuewen@hebut.edu.cn

xinliu9407@163.com

ss_gexiaoli@163.com

fanbinmeng@126.com

ABSTRACT:

The $\text{Sr}_2\text{CaWO}_6: \text{RE}^{3+}$ (RE = Dy, Sm and Eu) phosphors with the unusual emissions corresponding to the magnetic-dipole (MD) transition were synthesized via a sol-gel process. The crystal structure, electronic properties, photoluminescence excitation and emission spectra, and fluorescence lifetimes of the as-prepared samples were investigated. X-ray diffraction analysis confirmed that Sr_2CaWO_6 crystallized in the monoclinic structure with the centrosymmetric monoclinic space group ($\text{P}2_1/\text{n}$). The indirect band gap for Sr_2CaWO_6 was 4.24 eV, which was calculated within the framework of density functional theory (DFT). The phosphors could be excited by the ultra-violet (UV) light at 280 nm, and exhibited characteristic emissions corresponding to the MD transitions for different RE^{3+} ions. The WO_6 groups in the host lattice can absorb UV light efficiently, and then transferred the energy to activator ions. The results indicated that the doped rare earth ions occupied the centrosymmetric site in Sr_2CaWO_6 lattice. With increasing the concentration of the dopants, the local symmetry of the activator ions can be effectively changed, which resulted in the enhancement of the characteristic emissions dominated by the electric-dipole (ED) transitions of the doped RE^{3+} . The $\text{Sr}_2\text{CaWO}_6: \text{Sm}^{3+}$ phosphor exhibited near white emission under radiation of 280 nm.

Keywords: Double perovskite; Phosphors; Photoluminescence; WLEDs

1. INTRODUCTION

Because of the unique performances, such as long lifetime, low energy consumption, high efficiency, environmental friendliness and high safety coefficient, the white light-emitting diodes (WLEDs) have been considered as the fourth generation solid state lighting source [1-4]. Usually, there are two primary routes to generate white light from LED chip, i.e., the multi-LED chip method and the phosphor conversion method [5, 6]. Although the devices based on the former route usually exhibit higher quantum efficiency, the less stability and high cost limit its application. Hence the phosphor conversion method is widely used to fabricate WLEDs due to its practicability and low cost [7]. Obviously, phosphors play an important role in creating white light with satisfactory color rendering index (CRI) and high quantum efficiency (QE). The mostly common WLEDs are manufactured by combining a blue LED chip and a yellow-emitting cerium-doped yttrium aluminum garnet (YAG: Ce³⁺) phosphor. But these devices usually suffer from low CRI (Ra < 80) due to the lack of red emission in spectra [8-12]. To solve these problems, multiple phosphors are coupled to a blue LED to strengthen the red part of the spectrum [13]. Alternatively, white LEDs with high CRI performances can be achieved by pumping the multiple red/green/blue phosphors blend with an ultraviolet (UV) or a near-UV chip [14]. Of particular interest are the rare earth ions activated tungstates which usually exhibit high energy-conversion efficiency, excellent thermal and chemical stability [15, 16].

Recently, the compounds with the general formula of A₂B'B''O₆ and double perovskite structure have been intensively studied because of its interesting electrical, magnetic and optical properties for technological applications [17-19]. The double-perovskite structure can

be described as a three-dimensional network of alternating $B'O_6$ and $B''O_6$ octahedra, with A atoms occupying the interstitial locations. The most common A-site cations are the alkaline-earth or rare-earth elements with large radius, such as Ca, Sr, Ba and La. The B-site cations are usually transition metal elements with small radius. Due to the flexibility on structure and composition, the double perovskites have been considered as the potential hosts for the rare-earth ions activated phosphors. Usually, the tungstates and molybdates with double perovskite structure exhibit broad and strong absorption in near ultraviolet and blue region, which is suitable for blue or ultra-violet (UV) LED chips [20-22]. The emission spectra of phosphors can be effectively modulated by coupling different activators and hosts. The $Sr_2CaMoO_6: Sm^{3+}$ phosphors synthesized with the solid state reaction method were simultaneously excitable by UV and blue radiation, and exhibited white emission band consisted of three peaks located at 567, 603 and 650 nm [23]. The counterparts, the $Sr_2CaWO_6: Sm^{3+}$ phosphors, were excited under UV and violet light, and showed similar emission band with three peaks [24]. The $Sr_2CaMoO_6: Eu^{3+}$ phosphors exhibited the red emission at around 594 nm [25]. While, owing to the changing of local symmetry by the introduced Na^+ as charge compensator, the $Sr_2CaWO_6: Eu^{3+}, Na^+$ phosphors showed intense emission at 615 nm [26]. It is noted that the fluorescence of rare earth ions in these hosts is almost dominated by the electric dipole (ED) transitions. The dependence of photoluminescent properties on the composition of host was also studied for other double perovskites [27-30]. However, the systematic investigation on the photoluminescent properties of rare-earth ions doped Sr_2CaWO_6 is still absent.

In this work, the series of $Sr_2CaWO_6: RE^{3+}$ (RE = Dy, Sm and Eu) phosphors were

synthesized with a sol-gel method. The alkaline metal ion, Li^+ , was introduced as the charge compensator. The crystal structure of the tungstate was discussed with both experimental results and the first-principles calculations. The optical bandgap, excitation, emission and lifetime spectra of the as-prepared phosphors were studied. The unusual photoluminescence corresponding to the magnetic dipole (MD) transition was discussed.

2. Experimental and Calculation Details

2.1 Materials and Synthesis

The $\text{Sr}_2\text{CaWO}_6:\text{RE}^{3+}$ (RE = Dy, Sm and Eu) samples were prepared with the citric acid assisted sol-gel method using $\text{Sr}(\text{NO}_3)_2$, $\text{Ca}(\text{NO}_3)_2 \cdot 4\text{H}_2\text{O}$, $(\text{NH}_4)_6\text{W}_7\text{O}_{24} \cdot 6\text{H}_2\text{O}$, $\text{Sm}(\text{NO}_3)_3 \cdot 6\text{H}_2\text{O}$, Eu_2O_3 , Dy_2O_3 , $\text{LiOH} \cdot \text{H}_2\text{O}$, citric acid ($\text{C}_6\text{H}_8\text{O}_7 \cdot \text{H}_2\text{O}$, CA) and ethylenediaminetetraacetic acid (EDTA) as the raw materials. All the reagents were purchased from Shanghai Aladdin Reagent Co. Ltd. with analytic reagent. The oxides of rare earths were dissolved in the nitric acid solution with an appropriate concentration. The molar ratio of CA, EDTA and the total content of cations was selected as 2: 1: 1. Firstly, all the inorganic salts with the stoichiometric ratio were dissolved in deionized water at 65 °C. Secondly, CA and EDTA were added in the above solution in turn at 80 °C with strongly stirring to form transparent gel. The as-prepared gel was heated at 180 °C for 0.5 h in oven to obtain foam-like precursor powders. Thirdly, the precursor powders were sintered at 600°C for 4h in muffle furnace under air condition to remove the organics. Finally, the phosphors were fabricated by sintering the precursor powders at 1200°C for 6h under air condition.

2.2 Characterization

The phase compositions of the samples were analyzed using X-ray powder diffraction (XRD, Cu $K\alpha$, SmartLab, Riguka, Japan). The ultraviolet-visible diffuse reflectance spectra (DRS) of the as-prepared samples were recorded on an ultraviolet-visible spectrometer (UV-Vis, Hitachi U3900) at room temperature. The excitation and emission spectra were measured with a steady and transient state spectrophotometer (Horiba, FL-3-22).

2.3 Calculation Details

The crystal structure and electronic properties of Sr_2CaWO_6 were investigated with the first-principles calculations based on density functional theory (DFT). As reported by Gateshki et. al. [31], Sr_2CaWO_6 shows a rich polymorphism over a wide range of temperature. In the present work, we investigated the structural and electronic properties of Sr_2CaWO_6 crystallized in two different crystal structures, i.e. the orthorhombic structure with the space group of Pmm2 (No. 25) and the monoclinic structure with the space group of $P2_1/n$ (No. 14). Figure 1 illustrates the schematic diagrams of the unit cells for these two structures. For each structure, the full optimizations of both lattice constants and atomic coordinates, and the calculations electronic structures were carried out using the projector-augmented wave (PAW) method [32], as implemented in the Vienna ab initio simulation package (VASP) [33, 34]. The exchange-correlation functional was treated with the general gradient approximation (GGA) of Perdew-Burke-Ernzerhof (PBE) scheme [35]. The integration over the first Brillouin zone was performed with Monkhorst-Pack scheme and $6 \times 6 \times 5$ grid was used for k-point sampling. The $2s^2p^4$ electrons on O, the $3p^64s^2$ electronson Ca, the $4s^24p^65s^2$ electrons on Sr, and the $6s^25d^4$ electrons on W were explicitly treated as valence electrons. It is well known that DFT calculations usually underestimate the bandgap of a semiconductor. Therefore, we

employed screened hybrid functional with the screening parameter of 0.2 as prescribed by Heyd, Scuseria and Ernzerhof (HSE06) to accurately calculate the electronic structure of Sr_2CaWO_6 [36].

3. Results and Discussion

3.1 Crystal Structure

According to the investigation on the phase transformation of Sr_2CaWO_6 by Gateshki et al. [31], the crystal structure of this tungstate shows temperature-dependent evolution with the following sequence: $P2_1/n \rightarrow I4/m \rightarrow Fm\bar{3}m$. These two phase transitions occur at 1130 and 1250 K, respectively. In other words, Sr_2CaWO_6 crystallized in the monoclinic structure at room temperature rather than the orthorhombic structure (Pmm2), which had usually been adopted to describe the crystal structure of this tungstate in the original [37] and recent literatures [24, 26]. Thus, it is necessary to clarify the crystal structure of Sr_2CaWO_6 .

After the full geometry optimization with the DFT calculations, the symmetry of the unit cell of Sr_2CaWO_6 with orthorhombic structure changes from Pmm2 (No. 25) to Pmmn (No. 59). Furthermore, the optimized lattice constants of the optimized structure show relatively large deviation ($\sim 4\%$) from the experimental results [24]. According to both the experimental [31] and theoretical results, it is unreasonable to analyze the crystal structure of Sr_2CaWO_6 with the space group of Pmm2. As shown in Figure 1, the orthorhombic and monoclinic structures bear some resemblances to one another. The common nature is the presence of the WO_6 and CaO_6 octahedra in the unit cell. However, there are also some structural differences between these two phases. First, the WO_6 octahedra in the monoclinic

cell are distorted and unparallel to the lattice axis. Second, the angle of W-O-W in the distorted WO_6 octahedron deviates from 90° . Third, the Sr atoms in the monoclinic cell are located at the inside positions of the unit cell. Such differences could be also reflected in the XRD patterns of the as-prepared Sr_2CaWO_6 samples. Figure 2 (a) shows the experimental and refined profiles of the XRD patterns of Sr_2CaWO_6 in the $\text{P}2_1/\text{n}$ space group. The as-prepared sample is mainly composed of Sr_2CaWO_6 with tiny amount of SrWO_4 . The Rietveld refinements of the structural parameters were carried out using the General Structure Analysis System (GSAS) program [38]. The reliability factors of the refinement are $R_{\text{wp}} = 11.65\%$, $R_p = 8.55\%$ and $\chi^2 = 3.042$. As tabulated in Table I and II, the values of refined lattice constants and atomic coordinates are in good agreement with the calculated results and the previous study [31]. Hence, the refined results using a structure mode with the $\text{P}2_1/\text{n}$ space group are creditable. Furthermore, as shown in Figure 2 (b), the splitting of diffraction peaks at 2θ ranged from 63° to 65° is also observed in the XRD patterns, which cannot be deduced from the orthorhombic structure in the $\text{Pmm}2$ space group [31]. We also note that SrCaMoO_6 , the counterpart of Sr_2CaWO_6 , also has the space group of $\text{P}2_1/\text{n}$ [23]. In summary, the as-prepared Sr_2CaWO_6 powders crystallize in the monoclinic structure with the space group of $\text{P}2_1/\text{n}$ (No. 14).

Figure 3 illustrates the XRD patterns of the Dy^{3+} doped Sr_2CaWO_6 phosphors. All the XRD patterns of the as-prepared samples can be well indexed to the monoclinic Sr_2CaWO_6 . The diffraction peaks at $2\theta = 27.7^\circ$ belonged to the second phase of SrWO_4 can be observed [31, 39]. The XRD patterns of the other samples, including $\text{Sr}_2\text{CaWO}_6: \text{Sm}^{3+}$, $\text{Sr}_2\text{CaWO}_6: \text{Eu}^{3+}$, and $\text{Sr}_2\text{CaWO}_6: \text{RE}^{3+}, \text{Li}^+$, are similar to the above patterns, and are not shown here.

3.2 Electronic Structure

In the previous study, the electronic structure of the orthorhombic Sr_2CaWO_6 with the space group of $\text{Pmm}2$ had been investigated with the pseudopotential method using the GGA-PBE exchange-correlation functional [24]. However, to our best knowledge, the electronic structure of the monoclinic Sr_2CaWO_6 with the space group of $\text{P}2_1/\text{n}$ was still of lack. In the present work, the accurate results of the electronic structure were obtained with the HSE06 hybrid functional. Figure 4 displays the band structure of monoclinic Sr_2CaWO_6 . The plots of total and projected density of states are presented in Figure 5. The Fermi level was aligned at 0 eV. Obviously, the monoclinic Sr_2CaWO_6 is an indirect semiconductor with the band gap of 4.24 eV. The maximum of valence band (VBM) is mainly contributed by O 2p states, while the conduction band minimum (CBM) is dominated by W 5d state. Due to the structural analogy, these natures are similar to the results of the other perovskites [24, 40, 41].

Figure 6 shows the UV-Vis DRS of the as-prepared $\text{Sr}_2\text{CaWO}_6:\text{Dy}^{3+}$ phosphors. The undoped Sr_2CaWO_6 shows strong absorption in the UV light region with the absorption edge of ~ 320 nm. The optical band gap of Sr_2CaWO_6 can be estimated from the insert plot in Figure 6 using the following equation [42],

$$\alpha h\nu = A(h\nu - E_g)^{n/2} \quad (1)$$

where, E_g , a , ν , A are optical band gap, absorption coefficient, light frequency and a constant, respectively. The values of n for the direct and indirect semiconductors are 1 and 4, respectively. Herein, the value of n is equal to 4 for the monoclinic Sr_2CaWO_6 with the indirect gap. The calculated value of the optical band gap is 3.51 eV for Sr_2CaWO_6 , which is well agree with the previously experimental studies [24, 26]. According to the studies on the

optical properties of Sr_2WO_4 [43, 44], the optical band gap of the tungstate is strongly dependent on the preparation conditions, the microstructure and surface defects, etc. Furthermore, the theoretical value of the band gap of a semiconductor calculated with the hybrid functional is usually larger than the optical band gap derived from the UV-Vis DRS [45, 46]. In the present work, the DFT result of band gap for Sr_2CaWO_6 is 0.73 eV higher than the experimental one. For the Dy^{3+} and other rare earth ions doped Sr_2CaWO_6 phosphors, the add-on shoulder is imposed onto the cutoff edge of each spectrum, which extends the absorption range to about 460 nm. The introduction of the doped rare earth ions also result in the red shift of absorption edge. Hence, the dopants are effectively incorporated with Sr_2CaWO_6 and introduce the energy transfer from the host to the doped rare earth ions.

3.3 Photoluminescent Properties.

Figure 7 exhibits the photoluminescence excitation (PLE) and emission (PL) spectra of Sr_2CaWO_6 . A broad and symmetric emission band centered at 426 nm can be observed upon the excitation at 275 nm. The emission spectrum, which arises from the annihilation of self-trapped excitation in WO_6 octahedral complex, is similar to those of alkaline-earth tungstates with the perovskite structure [30, 44]. The broad band in blue wavelength region suggests that the emission process is a typical multi phonon process. In the other word, the relaxation from CBM to VBM of Sr_2CaWO_6 occurs by several paths, involving the coupling of several energy states within the band gap. The photoluminescence performance makes the tungstate suitable for the host of full-color-emitting phosphors under the excitation with near-UV.

In the present work, the comparative study on the photoluminescent property of Sr_2CaWO_6 : RE^{3+} (RE = Dy, Sm and Eu) was carried out. The photoluminescent property of these rare earth ions is sensitive to the locally chemical environment, and is further applied to discuss the local symmetry of the host. Figure 8 (a) presents the PLE and PL spectra of Sr_2CaWO_6 : 0.01 Dy^{3+} sample. The excitation spectrum monitored at 494 nm is composed of two parts, including the charge transfer (CT) band of the $\text{O}^{2-} - \text{W}^{6+}$ transition centered at 280 nm, and the weak peaks originated from the f-f transitions of Dy^{3+} ion. The peaks at 353, 365 and 455 nm are ascribed to the transitions of ${}^6\text{H}_{15/2} \rightarrow {}^6\text{P}_{7/2}$, ${}^6\text{H}_{15/2} \rightarrow {}^6\text{P}_{5/2}$, ${}^6\text{H}_{15/2} \rightarrow {}^4\text{I}_{15/2}$, respectively. It is noted that the intensity of CT band is much higher than those of characteristic peaks of Dy^{3+} ion, implying that the excitation energy can be effectively transferred from WO_6 octahedral complex to Dy^{3+} ion. The emission spectrum in Figure 8 (a) under the excitation of 280 nm also consists of two parts: one is the corresponding CT band with low intensity centered at 426 nm, the other is the peaks in blue (482 and 494 nm) and yellow (585 nm) wavelength region. The blue emissions are assigned to the magnetic dipole (MD) transition from ${}^4\text{F}_{9/2}$ to ${}^6\text{H}_{15/2}$ of Dy^{3+} ion, while the yellow emission is due to the forced electric dipole (ED) transition from ${}^4\text{F}_{9/2}$ to ${}^6\text{H}_{13/2}$ of Dy^{3+} ion [30]. The intensity of the peak at 494 nm is about five times higher than that of the peak at 585 nm. This result indicates that the doped Dy^{3+} ions are substituted at centrosymmetric site in host lattice [30]. As $\text{P}2_1/\text{n}$ is a centrosymmetric monoclinic space group, the finding further confirmed the creditability of the above structural analysis for Sr_2CaWO_6 .

Figure 8 (b) plots the dependence of emission intensity of the MD transition at 494 nm on the concentration of dopants in Sr_2CaWO_6 : $x \text{Dy}^{3+}$ and Sr_2CaWO_6 : $x\text{Dy}^{3+}$, $x\text{Li}^+$ ($x = 0.01 \sim 0.1$)

phosphors. The co-doped Li^+ ions were introduced as the charge compensators. The codoping of Li^+ ion in low concentration ($x = 0.005, 0.01$) nearly has no effects on the relative emission intensity of the MD transition to ED transition, implying the symmetry of Dy^{3+} ions in Sr_2CaWO_6 host is not varied. The optimum concentration of dopant is about 0.01. When the concentration of dopant (either monodoping of Dy^{3+} or codoping of Dy^{3+} and Li^+) is further increased beyond 0.01, the intensities of both blue and yellow emission gradually decrease. It is usually attributed to the nonradiative energy transfer among Dy^{3+} ions [24, 30, 44]. The critical distance (R_c) is also calculated to discover the average distance between the nearest trivalent Dy ions at which energy transfer occurs in $\text{Sr}_2\text{CaWO}_6: \text{Dy}^{3+}$ phosphors. The value of R_c can be estimated from the optimum concentration by using the following equation [47]

$$R_c = 2 \left(\frac{3V}{4\pi x_c N} \right)^{\frac{1}{3}} \quad (2)$$

where V is the volume of the unit cell, x_c is the optimum concentration of the activator ion, and N is the number of available crystallographic sites occupied by the activator ions in the unit cell. According to the above experimental results of V , x_c and N (276.447 \AA^3 , 0.01, 4), the R_c of Dy^{3+} in Sr_2CaWO_6 phosphors is calculated to be about 23.6 \AA . Therefore, the energy migration between Dy^{3+} ions is dominated when the distance between the Dy^{3+} ions in the host lattice is larger than the R_c .

As discussed above, the $\text{Sr}_2\text{CaWO}_6: \text{Dy}^{3+}$ phosphors exhibit dual-mode emission in blue and yellow wavelength region. However, the red emission in the spectrum is still of lack for full-color-emitting under the excitation of UV light. Meanwhile, it is also interesting to discover more MD emissions of other rare earth ions in Sr_2CaWO_6 host. Hence, two types of phosphors, including $\text{Sr}_2\text{CaWO}_6: \text{Sm}^{3+}$ and $\text{Sr}_2\text{CaWO}_6: \text{Eu}^{3+}$, were considered in the present

work. Figure 9 (a) shows the PLE and PL spectra of the $\text{Sr}_2\text{CaWO}_6: 0.03 \text{Sm}^{3+}$ sample. The excitation spectra are composed of the CT band and the narrow peaks originating from the f-f transitions of Sm^{3+} ions. These narrow peaks can be ascribed to the electronic transitions from ${}^6\text{H}_{5/2}$ to ${}^6\text{H}_{9/2}$ (346 nm), ${}^6\text{H}_{7/2}$ (355 nm), ${}^4\text{D}_{3/2}$ (364 nm), ${}^4\text{P}_{7/2}$ (378 nm), ${}^4\text{L}_{13/2}$ (407 nm), ${}^4\text{P}_{5/2}$ (420 nm), respectively [24, 48]. Similarly to the $\text{Sr}_2\text{CaWO}_6: \text{Dy}^{3+}$ samples, the intensity of the CT band is much higher than those of the characteristic excitation peaks of Sm^{3+} for the $\text{Sr}_2\text{CaWO}_6: \text{Sm}^{3+}$ samples. The PL emission spectrum consists of violet-blue emission band and the peaks originating from the transitions of ${}^4\text{G}_{5/2}$ excited state to ${}^6\text{H}_J$ ground states of Sm^{3+} , including ${}^4\text{G}_{5/2} \rightarrow {}^6\text{H}_{5/2}$ (564, 568, 577 nm), ${}^4\text{G}_{5/2} \rightarrow {}^6\text{H}_{7/2}$ (602, 616 nm) and ${}^4\text{G}_{5/2} \rightarrow {}^6\text{H}_{9/2}$ (648 nm).

In comparison with the previous studies [23, 24, 48], the PL and PLE spectra exhibit interesting differences in the present work. The first is that the excitation of $\text{Sr}_2\text{CaWO}_6: \text{Sm}^{3+}$ is dominated by the charge transfer of WO_6 octahedral complexes rather than the intrinsic f-f transition of Sm^{3+} . The second is that the relative intensities of the characteristic emission peaks of Sm^{3+} ion are obviously different from the reported results [24]. The ${}^4\text{G}_{5/2} \rightarrow {}^6\text{H}_{5/2}$ transition of Sm^{3+} is mainly magnetic-dipole-allowed, and the transition of ${}^4\text{G}_{5/2} \rightarrow {}^6\text{H}_{7/2}$ is of mixed ED and MD character. Whereas the ${}^4\text{G}_{5/2} \rightarrow {}^6\text{H}_{9/2}$ related emission of Sm^{3+} has a dominantly ED character [49]. For the $\text{Sr}_2\text{CaWO}_6: 0.03 \text{Sm}^{3+}$ sample (Figure 9 (a)), the intensity of MD related emission is much higher than that of ED dominated emission. On the contrary, the ED emission of the $\text{Sr}_2\text{CaWO}_6: \text{Sm}^{3+}$ samples synthesized with the solid-state reaction method is much more intense than the MD emission [24]. As shown in Figure 9 (b) and (c), with either increasing the concentration of Sm^{3+} or introducing the codoped Li^+ ions,

the intensity of the ED related emissions is enhanced, meanwhile MD dominated emission is suppressed. We adopted two intensity ratios, i.e. $I(^4G_{5/2} \rightarrow ^6H_{9/2})/I(^4G_{5/2} \rightarrow ^6H_{5/2})$ and $I(^4G_{5/2} \rightarrow ^6H_{7/2})/I(^4G_{5/2} \rightarrow ^6H_{5/2})$ (denoted as R_1 and R_2 , respectively) to discuss the above variation. The index R_1 is usually supposed as a measure for the polarizability of Sm^{3+} chemical environment or an indicator for the lattice distortion, i.e. the departure from centrosymmetry [50]. Owing to the partial ED feature of $^4G_{5/2} \rightarrow ^6H_{7/2}$ transition, the index R_2 can be also applied to characterize the chemical environment of Sm^{3+} . Figure 9 (d) shows the variations of R_1 and R_2 with the concentration of Sm^{3+} . The variation of these two ratios with the concentration of Sm^{3+} is similar to one another. The values of both R_1 and R_2 are much lower than the results reported by Wang *et al* [24], which implies that the site occupation of doped Sm^{3+} ions is significantly different in the present and previous studies. As mentioned above, the phosphors were synthesized using the sol-gel technique in this work, which was favorable for the formation of homogeneous mixture of all reactants in molecular scale. Hence, the doped rare earth ions could orderly replace A site cations in the host lattice with less distortion. In the case of $\text{Sr}_2\text{CaWO}_6:\text{Sm}^{3+}$, the doped Sm^{3+} ions occupy the centrosymmetric site with high symmetry, and thereby exhibit intense MD related emission. As the concentration of dopants increases, the host lattice is gradually distorted, which results in the deviation of the local symmetry of doped Sm^{3+} ions from the inversion symmetry. Thus, the MD related emission is depressed, and the ED emission is enhanced. The critical distance of Sm^{3+} ions in Sr_2CaWO_6 host was also estimated as 16.4 Å with equation (2). Accordingly, the photoluminescent properties of the $\text{Sr}_2\text{CaWO}_6:\text{Sm}^{3+}$ phosphors are strongly influenced by the preparation route.

It is well known that the ${}^5D_0 \rightarrow {}^7F_2$ transition of trivalent europium ion is hypersensitive to the local crystal environment of host lattice. Thus, the photoluminescent properties of $Sr_2CaWO_6: Eu^{3+}$ phosphors are investigated to further verify the effects of the synthesis method on the performance of the phosphor. Figure 10 (a) displays the PLE and PL spectra of the as-prepared $Sr_2CaWO_6: 0.05Eu^{3+}$ phosphor. The phosphor shows two strong red emission bands centered at around 595 and 616 nm, which are corresponding to the ${}^5D_0 \rightarrow {}^7F_1$ MD transition and ${}^5D_0 \rightarrow {}^7F_2$ ED transition, respectively [26-30]. Similar to the above results, under the excitation of UV light, the intensity of the MD related emission is much higher than that of ED transition. While, under the radiation of blue light at 465 nm, the ED emission is more intense than the MD one. As a result, the doped Eu^{3+} ions tend to occupy the inversion center sites with high symmetry. As shown in Figure 10 (b) and (c), the emission of ${}^5D_0 \rightarrow {}^7F_2$ transition can be effectively enhanced by increasing the content of Eu^{3+} or inducing the codoped Li^+ , which is also ascribed to the variation of local symmetry. Figure 10 (d) illustrates the red emission under the excitation of 465 nm for $Sr_2CaWO_6: Eu^{3+}, Li^+$ phosphors. Obviously, the dominated emission centered at 614 nm can be dramatically improved by the codoping of Li^+ [26]. For the Eu^{3+} doped Sr_2CaWO_6 phosphors, the critical distance for Eu^{3+} ions was estimated to be about 12.4 Å with equation (2).

To further investigate the energy transfer behavior of the as-prepared phosphors, the fluorescence lifetimes of $Sr_2CaWO_6: RE^{3+}$ phosphors were measured at room temperature. Figure 11(a) shows the decay curve of the ${}^4F_{9/2} \rightarrow {}^6H_{13/2}$ emission for Dy^{3+} at 494 nm under the excitation of 280 nm. Each of the five decay curves consists of a fast decay at initial stage and a subsequently slow decay with a long tail. The fast component of the decay curve for

$\text{Sr}_{2-x}\text{Dy}_x\text{CaWO}_6$ was well fitted using a mono-exponential formula and the lifetime was on the order of microseconds. The initial intensity of the fast part for the $\text{Sr}_{2-x}\text{Dy}_x\text{CaWO}_6$ phosphors increases with increasing the concentration of Dy^{3+} ion. This dramatically fast decay had also been observed in the other Dy^{3+} -activated phosphors [51]. The slow part fits well with the following double-exponential equation:

$$I(t) = A_1 \exp\left(-\frac{t}{\tau_1}\right) + A_2 \exp\left(-\frac{t}{\tau_2}\right) \quad (3)$$

where I is the luminescence intensity, t is time, A_1 and A_2 are fitting parameters, τ_1 and τ_2 are the slow and rapid decay time for exponential components, respectively. The average decay time (τ^*) can be determined with the equation as follows:

$$\tau^* = \frac{A_1\tau_1^2 + A_2\tau_2^2}{A_1\tau_1 + A_2\tau_2} \quad (4)$$

As indicated in Figure 11(a), the decay times of Dy^{3+} ions were determined to be 144, 127, 70, 37 and 14 μs for $\text{Sr}_{2-x}\text{Dy}_x\text{CaWO}_6$ with $x = 0.005, 0.01, 0.03, 0.05$ and 0.1 , respectively. The decay time sharply decreases with increasing Dy^{3+} doping concentrations beyond 1 %, which is in good agreement with the above discussion on the optimum concentration of Dy^{3+} . As illustrated below, the decay curves of the $\text{Sr}_2\text{CaWO}_6:\text{Sm}^{3+}$ and $\text{Sr}_2\text{CaWO}_6:\text{Eu}^{3+}$ phosphors are also fitted well into the double-exponential functions. The double-exponential decay behaviors of the activators are mainly attributed to the energy transfer from the donor to activators [52]. In other words, the behavior is originated from the energy transfer from the WO_6 octahedron to the rare earth ions. Upon UV excitation, an electron is excited from the valence band to the conduction band of Sr_2CaWO_6 . Then, the excitation energy is transferred directly from the WO_6 group to the corresponding levels of the doped rare-earth ions, which partially occupy the position of Sr^{2+} ions [24, 26]. Subsequently, the nonradiative relaxation is

occurred from the high energy level to the characteristic level (the ${}^4F_{9/2}$ level for Dy^{3+} , the ${}^4G_{5/2}$ level for Sm^{3+} and the 5D_0 level for Eu^{3+}). Finally, the intrinsic emissions of the activators occur. The other two explanations, including the inhomogeneous distribution of the doped ions in the host material and the difference in the decay behaviors of the doped ions at the surface and the ions in the core of the particles, have also been suggested for double-exponential decay [52].

Figure 11(b) and (c) depict the normalized decay curves for the ${}^4G_{5/2} \rightarrow {}^6H_{5/2}$ emission of Sm^{3+} and the ${}^5D_0 \rightarrow {}^7F_1$ transition of Eu^{3+} excited at 280 nm, respectively. The decay curves of these two rare earth ions are also well fitted with the double-exponential equation (3). Accordingly, the decay times were calculated and tabulated in Figure 11. When the $Sr_{2-x}Sm_xCaWO_6$ phosphors were excited with 280 nm pulsed light, the lifetimes of MD transition decreased with the increasing Sm^{3+} concentration. The shorten lifetimes implies that the cross relaxation may happen between Sm^{3+} ions due to its high concentration. As indicated in Figure 11 (c), the lifetimes of the ${}^5D_0 \rightarrow {}^7F_1$ emission of Eu^{3+} ion in Sr_2CaWO_6 host are much higher than those of the other rare earth ions. Furthermore, the lifetimes decrease slowly with increasing Eu^{3+} concentration up to 10 %. It can be attributed to that with increasing the concentration of doped Eu^{3+} ions, the density of the Eu^{3+} ions around the quenching center is enhanced, which can lead to a trap capture to resonance fluorescence transfer of the activator ions [53].

The emission color of the phosphors can be exactly determined with the international Commission on Illumination (CIE) chromaticity coordinates. Table III lists the CIE chromaticity coordinates calculated from the PL spectra of the $Sr_2CaWO_6: RE^{3+}$ phosphors.

The $\text{Sr}_2\text{CaWO}_6:\text{Dy}^{3+}$ phosphor exhibits bluish-green light with CIE coordinate of (0.18, 0.22). Under the excitation of 407 and 465 nm light, the Sm^{3+} and Eu^{3+} doped Sr_2CaWO_6 phosphors show the orange emission with the CIE coordinates of (0.47, 0.39) and (0.50, 0.40), respectively. It is interesting that the CIE coordinate of $\text{Sr}_2\text{CaWO}_6:\text{Sm}^{3+}$ is calculated to be (0.36, 0.30) under 280 nm excitation. The results indicate that the $\text{Sr}_2\text{CaWO}_6:\text{Sm}^{3+}$ phosphor is suitable for generating white emission by combining UV emitting chips.

4. CONCLUSIONS

A series of $\text{Sr}_2\text{CaWO}_6:\text{RE}^{3+}$ (RE = Dy, Sm and Eu) phosphors with different concentrations were synthesized by a sol-gel method. The results of both Rietveld refinement on the XRD patterns and DFT calculations indicate that Sr_2CaWO_6 crystallizes in the monoclinic structure with the space group of $\text{P}2_1/\text{n}$ (No. 14). The electronic structure of the monoclinic Sr_2CaWO_6 was accurately calculated with the HSE06 hybrid functional. The monoclinic Sr_2CaWO_6 is an indirect semiconductor with the band gap of 4.24 eV. The Dy^{3+} doped Sr_2CaWO_6 exhibits intense emission band centered at 494 nm under excitation at 280 nm. The dominated emission is ascribed to the ${}^4\text{F}_{9/2} \rightarrow {}^6\text{H}_{13/2}$ MD transition. Similarly, the main emission of the $\text{Sr}_2\text{CaWO}_6:\text{Sm}^{3+}$ and $\text{Sr}_2\text{CaWO}_6:\text{Eu}^{3+}$ phosphors are dominated by the ${}^4\text{G}_{5/2} \rightarrow {}^6\text{H}_{5/2}$ MD transition of Sm^{3+} and the ${}^5\text{D}_0 \rightarrow {}^7\text{F}_1$ MD transition of Eu^{3+} , respectively. All these results indicate that the doped rare earth ions occupy the centrosymmetric site in Sr_2CaWO_6 lattice, and further confirm the creditability of structural analysis for Sr_2CaWO_6 . The unique site occupation can be attributed to the sol-gel process applied in the present work. The relative intensity of the bands originated from different transitions is strongly dependent

upon the local chemical environment around RE^{3+} ions, which can be changed by increasing the concentration of the doped RE^{3+} and codoped Li^+ . The critical distance for energy migration between RE^{3+} pairs in Sr_2CaWO_6 host are estimated to be 23.6, 16.4 and 12.4 Å for Dy^{3+} , Sm^{3+} and Eu^{3+} , respectively. Furthermore, the appropriate CIE coordinate (0.36, 0.30) of $\text{Sr}_2\text{CaWO}_6: \text{Sm}^{3+}$ makes it suitable for generating white emission by combining UV emitting chips.

Acknowledgements

This work was supported by the Science and Technology Innovation Fund for Outstanding Youth in Hebei University of Technology (No. 2013006), the Natural Science Foundation of Hebei Province (No. E2014202155, E2018202085).

REFERENCES

- [1] R.S. Liu, Y.H. Liu, N.C. Bagkar, S.F. Hu. *Appl. Phys. Lett.* 91 (2007) L246.
- [2] A. Xie, X.M. Yuan, F.X. Wang, Y. Shi, Z.F. Mu. *J. Phys. D: Appl. Phys.*, 43 (2010) 55101.
- [3] Y.T. Li, X.H. Liu. *Mater. Res. Bull.* 64 (2015) 88-92.
- [4] Z.H. Wu, J. Liu, Q.J. Guo, M.L. Gong. *Chem. Lett.* 37 (2008) 190-191.
- [5] S.A. Pardhi, V.R. Panse, S.J. Dhoble. *Luminescence* 31 (2016) 1290-1294.
- [6] K.V. Dabre, S.J. Dhoble. *J. Lumin.* 150 (2014) 55-58.
- [7] G.H. Lee, T.H. Kim, C. Yoon, S. Kang. *J. Lumin.* 128 (2008) 1922-1926.
- [8] R.J. Xie, N. Hirotsaki, Y.Q. Li, T. Takeda. *Materials* 3 (2010) 3777-3793
- [9] S. Neeraj, N. Kijima, A.K. Cheetham. *Chem. Phys. Lett.* 387 (2004) 2-6.
- [10] S.Z. Ma, W.L. Feng, R. Chen, Z.Q. Peng. *J. Alloys Comp.* 700 (2017) 49-53
- [11] X.Y. Sun, J.H. Zhang, X. Zhang, S.Z. Lu, X.J. Wang. *J. Lumin.* s122-123 (2007) 955-957.
- [12] H.Y. Li, H.K. Yang, B.K. Moon, B.C. Choi, J.H. Jeong, K. Jang, H.S. Lee, S.S. Yi. *J. Alloys Comp.* 509 (2011) 8788-8793.
- [13] X.S. Yan, W.W. Li, X.B. Wang, K. Sun. *J. Electrochem. Soc.* 159 (2012) H195-H200.
- [14] X. Feng, W.L. Feng, M. Xia, K. Wang, H.G. Liu, D.S. Deng, X. Qing, W.K. Yao, W.T. Zhu. *RSC Adv.* 6 (2016) 14826-14831.
- [15] K. Wang, X. Feng, W.L. Feng, S.S. Shi, Y. Li, C. Zhang. *Z. Naturforsch.* 71 (2016) 21-25.
- [16] K. Wang, W.L. Feng, X. Feng, Y. Li, P. Mi, S.S. Shi. *Spectrochim. Acta A* 154 (2016) 72-75.
- [17] N.N. Li, B. Manoun, L. Tang, F. Ke, F.L. Liu, H.N. Dong, P. Lazor, W.G. Yang. *Inorg. Chem.* 55 (2016) 6770-6775.
- [18] Y.A. Alsbah, A.A. Elbadawi, E.M. Mustafa, M.A. Siddig. *J. Mater. Sci. Chem. Eng.* 4 (2016) 61-70.
- [19] S. Vasala, M. Karppinen. *Prog. Solid State Chem.* 43 (2015) 1-36.
- [20] R.P. Cao, X.F. Ceng, J.J. Huang, X.W. Xia, S.L. Guo, J.W. Fu. *Ceram. Inter.* 42 (2016) 16817-16821.
- [21] R.P. Cao, H.D. Xu, W.J. Luo, Z.Y. Luo, S.L. Guo, F. Xiao, H. Ao. *Mater. Res. Bull.* 81 (2016) 27-32.
- [22] A. Boukerika, L. Guerbous. *J. Lumin.* 145 (2014) 148-153.
- [23] L.L. Wang, H.M. Noh, B.K. Moon, S.H. Park, K.H. Kim, J.S. Shi, J.H. Jeong. *J. Phys. Chem. C* 119 (2015) 15517-15525.
- [24] L.L. Wang, B.K. Moon, S.H. Park, J.H. Kim, J.S. Shi, K.H. Kim, J.H. Jeong. *Rsc Adv.* 5 (2015) 89290.
- [25] Z.G. Xia, J.F. Sun, H.Y. Du, D. Chen, J.Y. Sun. *J. Mater. Sci.* 45 (2010) 1553-1559.
- [26] Y. Yang, L. Wang, P. Huang, Q.F. Shi, Y. Tian, C.E. Cui. *Polyhedron* 129 (2017) 65-70.
- [27] Y.Y. Ma, W.G. Ran, W.N. Li, C.Y. Ren, H.Y. Jiang, J.S. Shi. *Luminescence*, 31 (2015) 665-670.
- [28] X.L. Zhang, Z.S. Li, H.T. Zhang, S.X. Ouyang, Z.G. Zou. *J. Alloys Comp.* 469 (2009) L6-L9.
- [29] L. Li, Y. Pan, X.J. Zhou, C.L. Zhao, Y.J. Wang, S. Jiang, A. Suchocki, M.G. Brik. *J. Alloys Comp.* 685 (2016) 917-926.
- [30] K.V. Dabre, K. Park, S.J. Dhoble. *J. Alloys Comp.* 617 (2014) 129-134.
- [31] M. Gatashki, J.M. Igartua. *J. Phys.: Condens. Matter* 16 (2004) 6639-6650.
- [32] P.E. Blöchl. *Phys. Rev. B* 50 (1994) 17953.
- [33] G. Kresse, J. Furthmuller. *Comput. Mater. Sci.* 6 (1996) 15-50.

- [34] G. Kresse, D. Joubert. *Phys. Rev. B* 59 (1999) 1758-1775.
- [35] J.P. Perdew, K. Burke, M. Ernzerhof. *Phys. Rev. Lett.* 77 (1996) 3865.
- [36] J. Heyd, G.E. Scuseria, M. Ernzerhof. *J. Chem. Phys.* 118 (2003) 8207
- [37] Z.M. Fu, W.X. Li, D.C. Liang. *Sci. China A* 826 (1983) 835-847.
- [38] A.C. Larson, R.B. Von Dreele. *GSAS – General Structure Analysis System*. Los Alamos, USA, 1998.
- [39] Y. Li, X.Z. Li, X.T. Wei, Z.Y. Li, H.M. Chen, W.M. Wang, W. Zhao, Y.X. Ji. *Infrared Phys. Techn.* 77 (2016) 40-44.
- [40] B. Modak, K. Srinivasu, S. K. Ghosh. *J. Phys. Chem. C* 118 (2014) 10711-10719.
- [41] S. Wang, X.W. Xu, H. Luo, Y.H. Bai, S. Abbas, J. Zhang, J.L. Zhao. *J. Alloys Comp.* 681 (2016) 225-232.
- [42] D.L. Wood, J. Tauc. *Phys. Rev. B* 5 (1972) 3144.
- [43] Z.C. Shan, Y.M. Wang, H.M. Ding, F.Q. Huang. *J. Mol. Cata. A: Chem.* 302 (2009) 54-58.
- [44] J.C. Sczancoski, L.S. Cavalcante, M.R. Joya, J.W.M. Espinosa, P.S. Pizania, J.A.Varela, E. Longo. *J. Colloid Interf. Sci.* 330 (2009) 227-236.
- [45] Q.J. Liu, N.C. Zhang, F.S. Liu, H.Y. Wang, Z.T. Liu. *Opt. Mater.* 35 (2013) 2629-2637.
- [46] H.L. Shi, H. Pan, Y.W. Zhang, B.I. Yakobson. *Phys. Rev. B* 87 (2013) 155304.
- [47] G. Blasse. *Philips Res. Rep.* 24 (1969) 131–144.
- [48] E. Cavalli. *J. Lumin.* 183 (2017) 173-177.
- [49] C. Tiseanu, B. Cojocaru, D. Avram, V.I. Parvulescu, A.V. Vela-Gonzalez, M. Sanchez-Dominguez. *J. Phys. D: Appl. Phys.* 46 (2013) 275302.
- [50] A. Lupei, C. Tiseanu, C. Gheorghe, F. Voicu. *Appl. Phys. B* 108 (2012) 909
- [51] R. Zhang, X. Wang. *J. Alloys Comp.* 509 (2011) 1197–1200.
- [52] K. G. Sharma, N. R. Singh. *New J. Chem.* 37 (2013) 2784–2791.
- [53] E. Snoeks, P.G. Kik, *Opt. Mater.* 5 (1996) 159–167.

Table and Figure Captions

Table I Summary of the lattice constants and cell volume of the Sr_2CaWO_6 with the space group of $\text{P2}_1/\text{n}$.

Table II DFT calculated and refinement results of crystal structure for Sr_2CaWO_6 at room temperature. The atomic positions (in fractional coordinates) were refined in the space group of $\text{P2}_1/\text{n}$.

Table III CIE chromaticity coordinates of the Sr_2CaWO_6 : RE^{3+} samples.

Figure 1 Schematic diagrams of the unit cell of Sr_2CaWO_6 with different space group of (a) $\text{Pmm}2$ (No. 25) and (b) $\text{P2}_1/\text{n}$ (No. 14). The brown and green octahedrons represent WO_6 and CaO_6 complexes, respectively.

Figure 2 (a) Observed (Obs.), calculated (Calc.) and difference (Diff.) diffraction profiles for the Rietveld refinement of XRD patterns of the as-prepared Sr_2CaWO_6 samples at room temperature using the reported unit cell with the $\text{P2}_1/\text{n}$ space group. The background (Bckgr.) curve was plotted with the green line. (b) Enlarged profiles of the XRD patterns of Sr_2CaWO_6 .

Figure 3 The X-ray diffraction patterns of the $\text{Sr}_{2-x}\text{Dy}_x\text{CaWO}_6$ samples.

Figure 4 Band structure of monoclinic Sr_2CaWO_6 along the point with high symmetry in the Brillouin zone. The horizontal dashed line represents the Fermi level.

Figure 5 Total and projected density of the states of Sr_2CaWO_6 . The vertical dashed line indicates the Fermi level.

Figure 6 UV-Vis diffuse reflectance spectra of the Sr_2CaWO_6 and Dy^{3+} -doped Sr_2CaWO_6 samples with different concentrations. The insert is the plot of $(\alpha h\nu)^{1/2}$ vs. photon energy

(hv) for undoped Sr_2CaWO_6 .

Figure 7 PL excitation spectra and emission spectra of Sr_2CaWO_6 monitored at the 426 and 275 nm, respectively.

Figure 8 (a) PL excitation and emission spectra of the $\text{Sr}_{1.99}\text{Dy}_{0.01}\text{CaWO}_6$ sample. (b) Dependence of the emission intensity at 494 nm on the concentration of dopants for the $\text{Sr}_{2-x}\text{Dy}_x\text{CaWO}_6$ and $\text{Sr}_{2-2x}\text{Dy}_x\text{Li}_x\text{CaWO}_6$ samples.

Figure 9 (a) PL and PLE spectra of the $\text{Sr}_{1.97}\text{Sm}_{0.03}\text{CaWO}_6$ sample. (b) PL spectra of the $\text{Sr}_{2-x}\text{Sm}_x\text{CaWO}_6$ sample with different concentration of Sm^{3+} under the radiation of 280 nm. (c) PL spectra excited at 280 nm for the Sm^{3+} , Li^+ codoped Sr_2CaWO_6 samples. (d) Dependence of R_1 ($I(^4\text{G}_{5/2} \rightarrow ^6\text{H}_{9/2})/I(^4\text{G}_{5/2} \rightarrow ^6\text{H}_{5/2})$) and R_2 ($I(^4\text{G}_{5/2} \rightarrow ^6\text{H}_{7/2})/I(^4\text{G}_{5/2} \rightarrow ^6\text{H}_{5/2})$) on the concentration of Sm^{3+} .

Figure 10 (a) PL and PLE spectra of the $\text{Sr}_{1.95}\text{Eu}_{0.05}\text{CaWO}_6$ sample. (b) PL spectra of the $\text{Sr}_2\text{CaWO}_6: x\text{Eu}^{3+}$ phosphors under the excitation of 280 nm. (c) PL spectra of the Eu^{3+} , Li^+ codoped Sr_2CaWO_6 phosphors under the radiation of UV light at 280 nm. (d) PL spectra excited at 465 nm for the Eu^{3+} , Li^+ codoped Sr_2CaWO_6 phosphors.

Figure 11 (a) The fluorescence decay curves of the $^4\text{F}_{9/2} \rightarrow ^6\text{H}_{13/2}$ emission for Dy^{3+} monitored at 494 nm for the $\text{Sr}_2\text{Dy}_{2-x}\text{CaWO}_6$ samples with different Dy^{3+} concentrations. (b) The fluorescence decay curves of the for the $^4\text{G}_{5/2} \rightarrow ^6\text{H}_{5/2}$ emission of Sm^{3+} monitored at 568 nm for the $\text{Sr}_2\text{Sm}_{2-x}\text{CaWO}_6$ samples. (c) The decay curves for the $^5\text{D}_0 \rightarrow ^7\text{F}_1$ transition of Eu^{3+} monitored at 595 nm. All curves are measured under the excitation of 280 nm at room temperature. The inserts tabulate the lifetimes of the phosphors calculated with the double-exponential equation.

Table I Summary of the lattice constants and cell volume of the Sr_2CaWO_6 with the space group of $\text{P2}_1/\text{n}$.

	a (Å)	b (Å)	c (Å)	β (°)	V (Å ³)
Cal.	5.7311	5.8665	8.1656	90.168	274.649
Exp.	5.7663	5.8480	8.1923	90.140	276.255
Ref.[29]	5.7672	5.8506	8.1931	90.165	276.447

Table II DFT calculated and refinement results of crystal structure for Sr_2CaWO_6 at room temperature. The atomic positions (in fractional coordinates) were refined in the space group of $P2_1/n$.

Atom	Wyckoff Position	x	y	z
Rietveld Refined				
W	2a	0.0000	0.0000	0.0000
Ca	2b	0.0000	0.0000	0.5000
Sr	4e	0.0101	0.5468	0.2561
O1	4e	0.0877	0.0271	0.7843
O2	4e	0.2631	0.8230	0.0420
O3	4e	0.1892	0.2711	0.0504
DFT Calculated				
W	2a	0.0000	0.0000	0.0000
Ca	2b	0.0000	0.0000	0.5000
Sr	4e	0.0099	0.5442	0.2516
O1	4e	0.0846	0.0284	0.7731
O2	4e	0.2690	0.8125	0.0408
O3	4e	0.1831	0.2677	0.0491

Table III CIE chromaticity coordinates of the $\text{Sr}_2\text{CaWO}_6:\text{RE}^{3+}$ samples.

Phosphor	Excitation wavelength (nm)	CIE coordinate
Sr_2CaWO_6	275	(0.12, 0.08)
$\text{Sr}_2\text{CaWO}_6:\text{Dy}^{3+}$	280	(0.18, 0.22)
$\text{Sr}_2\text{CaWO}_6:\text{Eu}^{3+}$	285	(0.43, 0.28)
	465	(0.50, 0.44)
$\text{Sr}_2\text{CaWO}_6:\text{Sm}^{3+}$	280	(0.36, 0.30)
	407	(0.47, 0.39)

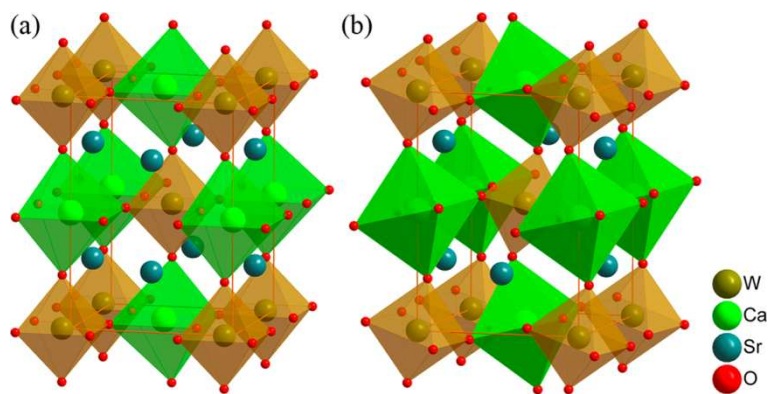


Figure 1 Schematic diagrams of the unit cell of Sr_2CaWO_6 with different space group of (a) Pmm2 (No. 25) and (b) $\text{P2}_1/\text{n}$ (No. 14). The brown and green octahedrons represent WO_6 and CaO_6 complexes, respectively.

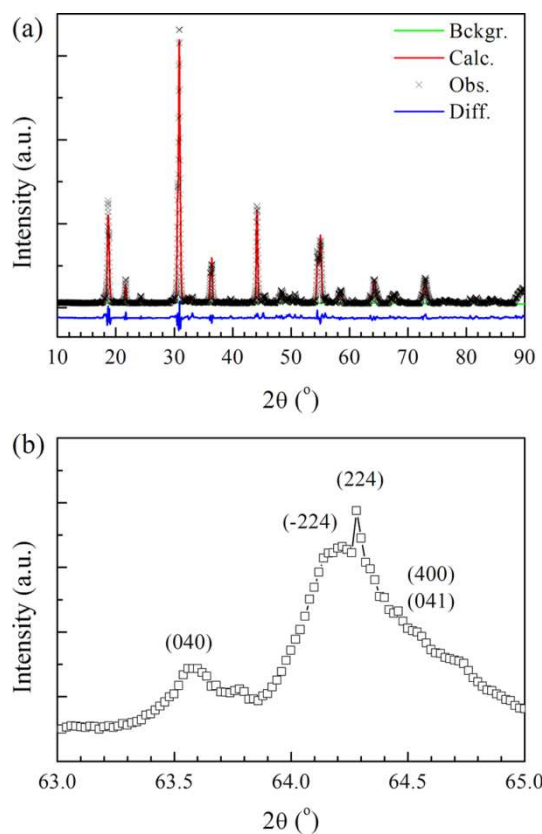


Figure 2 (a) Observed (Obs.), calculated (Calc.) and difference (Diff.) diffraction profiles for the Rietveld refinement of XRD patterns of the as-prepared Sr_2CaWO_6 samples at room temperature using the reported unit cell with the $P2_1/n$ space group. The background (Bckgr.) curve was plotted with the green line. (b) Enlarged profiles of the XRD patterns of Sr_2CaWO_6 .

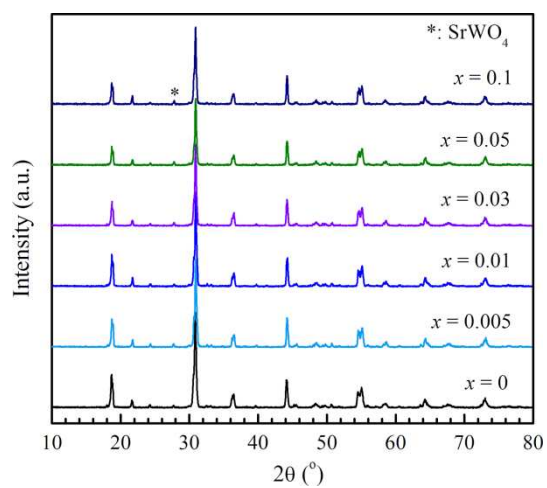


Figure 3 The X-ray diffraction patterns of the $\text{Sr}_{2-x}\text{Dy}_x\text{CaWO}_6$ samples.

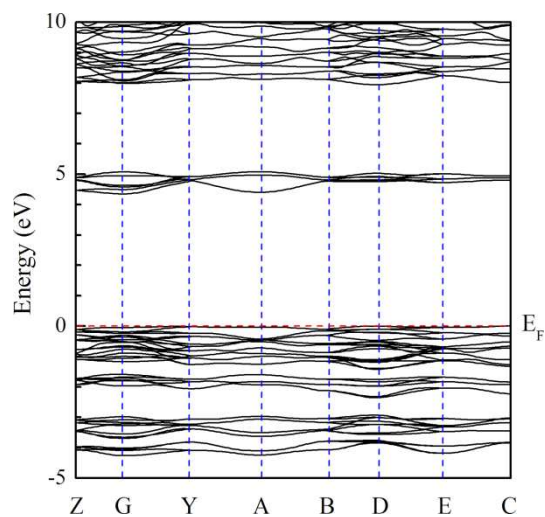


Figure 4 Band structure of monoclinic Sr₂CaWO₆ along the point with high symmetry in the Brillouin zone. The horizontal dashed line represents the Fermi level.

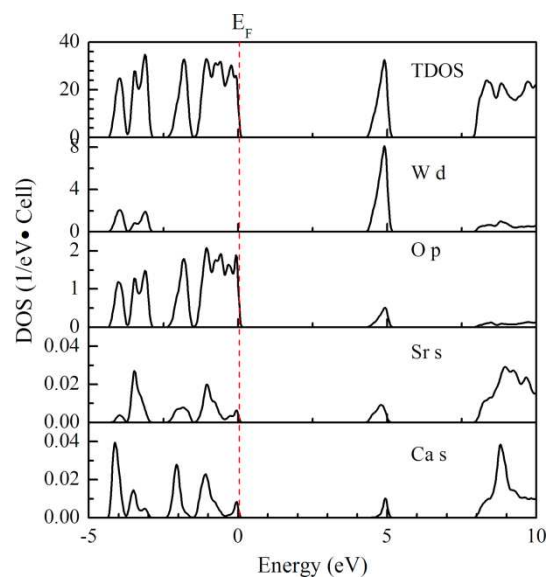


Figure 5 Total and projected density of the states of Sr_2CaWO_6 . The vertical dashed line indicates the Fermi level.

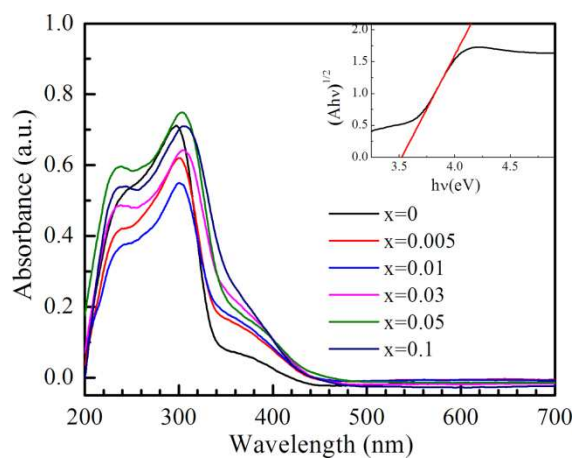


Figure 6 UV-Vis diffuse reflectance spectra of the Sr_2CaWO_6 and Dy^{3+} -doped Sr_2CaWO_6 samples with different concentrations. The insert is the plot the of $(\alpha h\nu)^{1/2}$ vs. photon energy $(h\nu)$ for undoped Sr_2CaWO_6 .

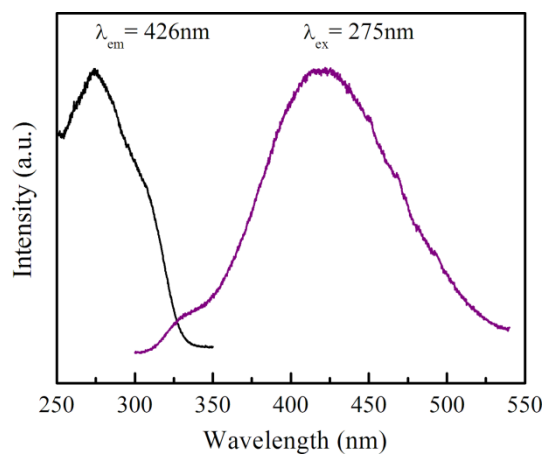


Figure 7 PL excitation spectra and emission spectra of Sr₂CaWO₆ monitored at the 426 and 275 nm, respectively.

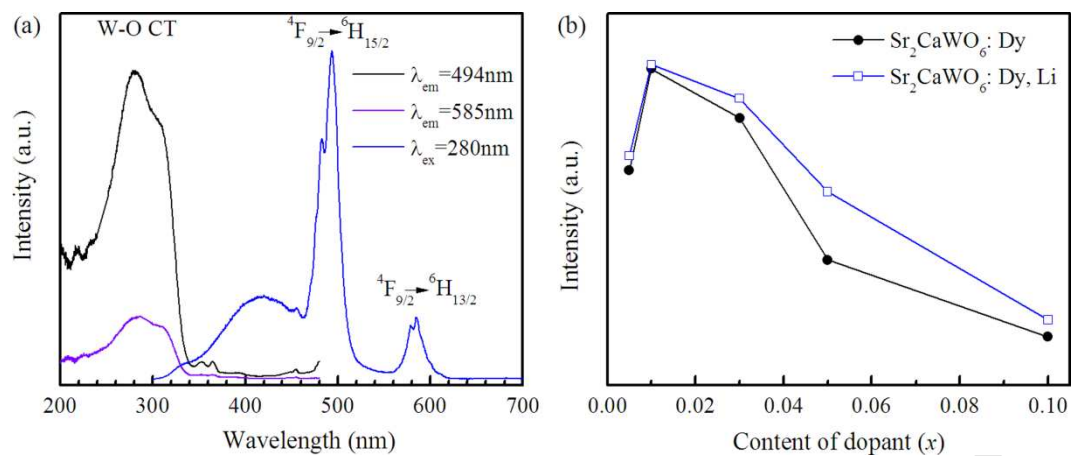


Figure 8 (a) PL excitation and emission spectra of the $\text{Sr}_{1.99}\text{Dy}_{0.01}\text{CaWO}_6$ sample. (b)

Dependence of the emission intensity at 494 nm on the concentration of dopants for the

$\text{Sr}_{2-x}\text{Dy}_x\text{CaWO}_6$ and $\text{Sr}_{2-2x}\text{Dy}_x\text{Li}_x\text{CaWO}_6$: samples.

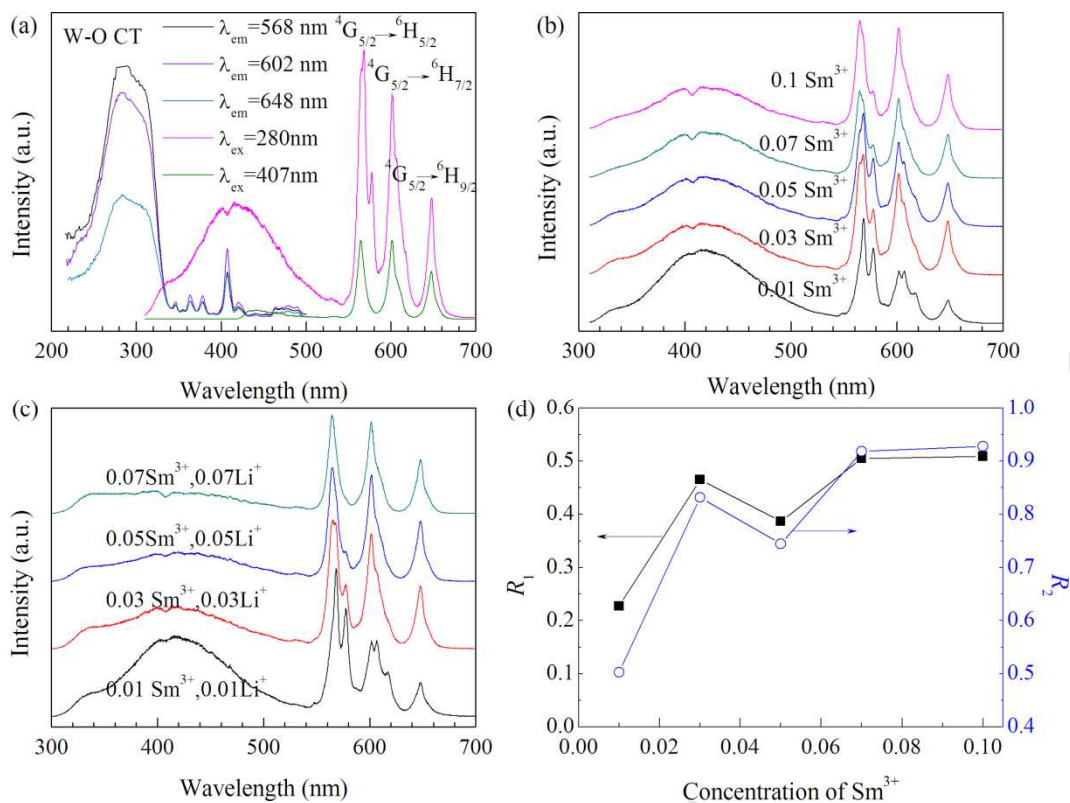


Figure 9 (a) PL and PLE spectra of the Sr_{1.97}Sm_{0.03}CaWO₆ sample. (b) PL spectra of the Sr_{2-x}Sm_xCaWO₆ sample with different concentration of Sm³⁺ under the radiation of 280 nm. (c) PL spectra excited at 280 nm for the Sm³⁺, Li⁺ codoped Sr₂CaWO₆ samples. (d) Dependence of R_1 ($I({}^4G_{5/2} \rightarrow {}^6H_{9/2})/I({}^4G_{5/2} \rightarrow {}^6H_{5/2})$) and R_2 ($I({}^4G_{5/2} \rightarrow {}^6H_{7/2})/I({}^4G_{5/2} \rightarrow {}^6H_{5/2})$) on the concentration of Sm³⁺.

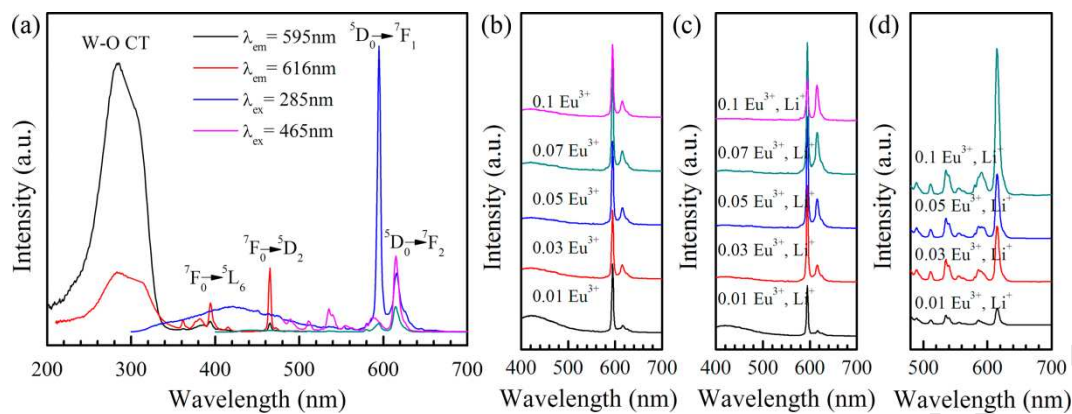


Figure 10 (a) PL and PLE spectra of the $\text{Sr}_{1.95}\text{Eu}_{0.05}\text{CaWO}_6$ sample. (b) PL spectra of the $\text{Sr}_2\text{CaWO}_6: x\text{Eu}^{3+}$ phosphors under the excitation of 280 nm. (c) PL spectra of the Eu^{3+} , Li^+ codoped Sr_2CaWO_6 phosphors under the radiation of UV light at 280 nm. (d) PL spectra excited at 465 nm for the Eu^{3+} , Li^+ codoped Sr_2CaWO_6 phosphors.

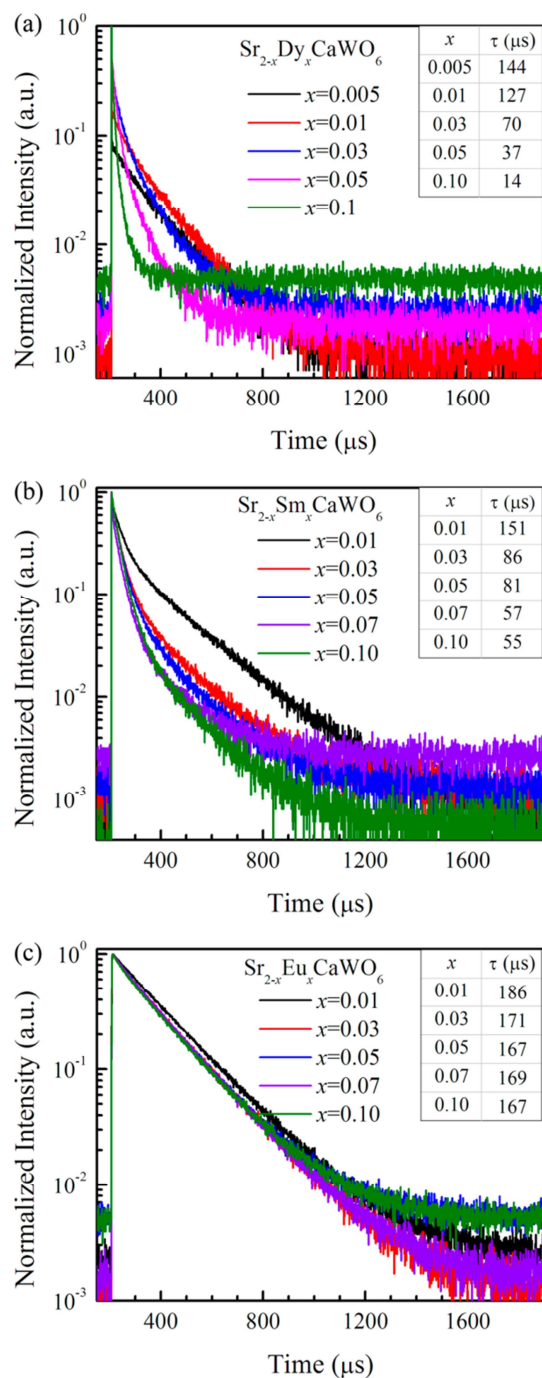


Figure 11 (a) The fluorescence decay curves of the ${}^4\text{F}_{9/2} \rightarrow {}^6\text{H}_{13/2}$ emission for Dy^{3+} monitored at 494 nm for the $\text{Sr}_2\text{Dy}_{2-x}\text{CaWO}_6$ samples with different Dy^{3+} concentrations. (b) The fluorescence decay curves of the for the ${}^4\text{G}_{5/2} \rightarrow {}^6\text{H}_{5/2}$ emission of Sm^{3+} monitored at 568 nm for the $\text{Sr}_2\text{Sm}_{2-x}\text{CaWO}_6$ samples. (c) The decay curves for the ${}^5\text{D}_0 \rightarrow {}^7\text{F}_1$ transition of Eu^{3+} monitored at 595 nm. All curves are measured under the excitation of 280 nm at room temperature. The inserts tabulate the lifetimes of the phosphors calculated with the double-exponential equation.

Highlights:

- 1) The as-prepared Sr_2CaWO_6 sample crystallizes in the monoclinic structure.
- 2) The PL emission of $\text{Sr}_2\text{CaWO}_6: \text{RE}^{3+}$ is dominated by MD transitions of RE^{3+} .
- 3) The doped RE^{3+} ions occupy the centrosymmetric sites of Sr_2CaWO_6 host.
- 4) The CIE coordinate of $\text{Sr}_2\text{CaWO}_6: \text{Sm}^{3+}$ is (0.36, 0.30).